Tectonophysics 502 (2011) 328–335

Contents lists available at ScienceDirect

Tectonophysics

journal homepage: www.elsevier.com/locate/tecto

Coseismic deformation of the 2010 Jiashian, Taiwan earthquake and implications for fault activities in southwestern Taiwan

Ya-Ju Hsu *, Shui-Beih Yu, Long-Chen Kuo, Yi-Chun Tsai, Horng-Yue Chen

Institute of Earth Sciences, Academia Sinica, P.O. Box 1–55, Nankang, Taipei, Taiwan

ARTICLE INFO

Article history:
Received 26 August 2010
Received in revised form 31 January 2011
Accepted 6 February 2011
Available online 14 February 2011

Keywords:
Jiashian earthquake
Coseismic slip distribution
GPS
Coulomb stress change

ABSTRACT

The March 04, 2010, Jiashian, Taiwan earthquake (M_w 6.4) ruptured an unknown fault at depth in southwestern Taiwan. The main shock initiated near the town of Liuquei at 23 km depth and the rupture propagated westward. Measurements of coseismic displacements from Taiwan Continuous GPS Array indicate horizontal displacements of 5–27 mm in the NW–SW directions to the west of the epicenter; while horizontal movements to the east of the epicenter are absent. The GPS vertical displacements show an uplift motion of about 5–25 mm near the epicenter, in contrast to a small movement of about 5–10 mm observed in the far-field GPS sites. We use coseismic GPS displacements and an elastic half-space dislocation model to invert for fault geometries and coseismic slip distribution associated with the Jiashian earthquake. Our preferred model exhibits 0.05–0.1 m of reverse slip and ~0.04 m of left-lateral slip on a N324°-trending fault with dip of 40° to NE, consistent with the earthquake focal mechanisms from BATS, USGS/NEIC, and Global CMT. The highest slip of 0.12 m mainly occurs to the west of the epicenter at a depth range of 15–20 km. Given the rigidity modulus of 60 GPa, the geodetic moment is 4.95×10^{18} N-m, equivalent to a M_w 6.4 earthquake and consistent with the seismic moment estimated from seismic waveform inversion. Additionally, we notice that the mainshock rupture area is surrounded by high seismicity between 1991 and 2007, suggesting that the Jiashian earthquake may be triggered by the high stress concentration in the vicinity. The calculated Coulomb stress changes on nearby fault systems imparted by the coseismic slip suggest that the Jiashian earthquake may encourage failures on the Chukou fault and inhibit ruptures on the Hsinhua fault. However, the Coulomb stress changes are more complicated on the Chaochou fault and Chishan fault with both positive and negative stress changes.

1. Introduction

The March 4, 2010 Jiashian earthquake (M_w 6.4) occurred about 5 km east of the Chaochou fault which represents the tectonic boundary of the Taiwan orogenic belt between the metamorphosed slate belt to the east and the foreland fold-and-thrust belt to the west (Ho, 1986). The Chaochou fault is a N–S trending high-angle oblique sinistral thrust fault. However, focal mechanism of the Jiashian earthquake show thrust faulting with two nodal planes of NE–SW striking, NW dipping; and NW–SE striking, NE dipping faults, respectively (Huang et al., in press; Lee et al., in press). Thus the causative fault of the Jiashian earthquake is not likely related to the Chaochou fault, but rather is an unknown fault which has not been discovered in southwestern Taiwan. The main shock initiated near the town Liuquei at 23 km depth and the rupture propagated westward (Fig. 1A). The occurrence of the Jiashian earthquake draws attention to the seismic hazard inducing by blind faults in southwestern Taiwan. It is of interest to study the pattern of coseismic displacement and fault geometry associated with the Jiashian earthquake and investigate potential seismic hazard in this region.

In this study, we firstly examine the GPS velocity field, seismicity, and earthquake focal mechanisms before the mainshock and give a general overview of the regional tectonic setting. We then use coseismic GPS displacements of the Jiashian earthquake simultaneously inverting for the coseismic slip distributions and fault geometries. The optimal coseismic slip model is used to calculate Coulomb stress changes on nearby fault systems and evaluate the seismic hazard in the area.

2. Preseismic Deformation and Seismicity

We examine the GPS velocity field between 2005 and 2009 in southern Taiwan before the Jiashian earthquake. The velocity with respect to a continuous GPS site, S01R, at Paisha, Penghu, decreases from ~50 mm/yr near the epicenter of the Jiashian earthquake to 20–50 mm/yr to the west of the epicenter (Fig. 1A) with the vectors close to E–W directed near the epicenter. Limited by insufficient GPS sites to

* Corresponding author. Tel.: +886 2 27839910x415; fax: +886 2 27883493.
E-mail address: yaru@earth.sinica.edu.tw (Y.-J. Hsu).

0040-1951/$ – see front matter © 2011 Elsevier B.V. All rights reserved.
doi:10.1016/j.tecto.2011.02.005

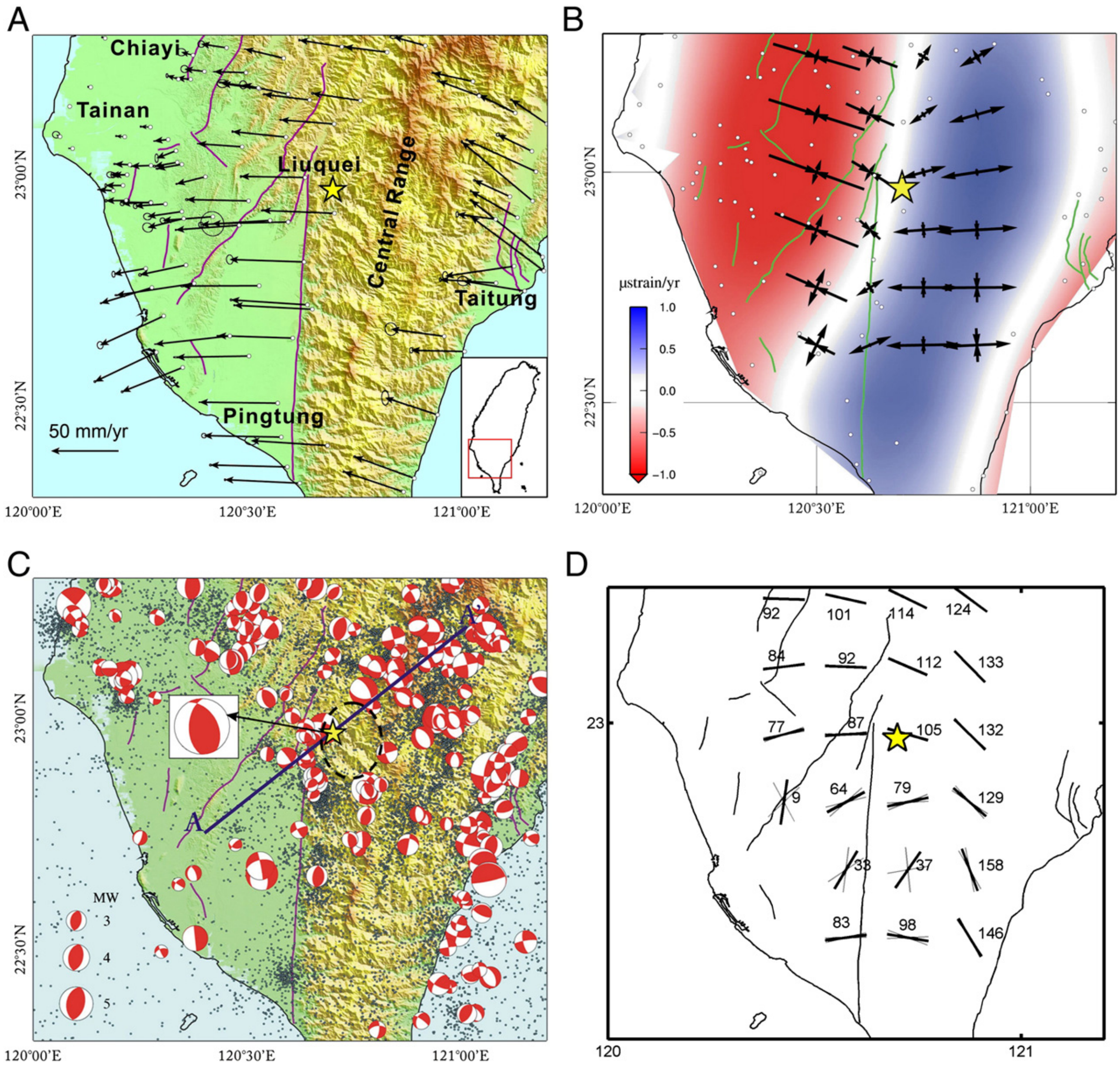

Fig. 1. GPS velocity and seismicity before the 2010 Jiashian earthquake. (A) GPS velocities with respect to Paisha, Penghu between 2005 and 2009 are shown in black vectors with 95% confidence ellipses. The color shaded relief indicates the topography. The star denotes the epicenter of the Jiashian earthquake. Major faults are indicated as purple lines. (B) Dilatation and principal strain rates. The color scale indicates dilatation rate in μstrain/yr. Black vectors denote the two principal strain-rate axes. (C) Black dots show the seismicity between 1991 and 2007 with magnitude larger than 2. Black ellipse indicates a seismic gap. The focal mechanisms with depth less than 40 km are from Wu et al. (2010) and their sizes are proportional to magnitude. The mainshock focal mechanism is from Huang et al. (in press). (D) The trend of the maximum horizontal compressive stress axes (S_H). Black texts indicate azimuths counted clockwise from the north.

the east of the epicenter in the Central Range, the deformation in the mountain area is not clear. To the region further east, GPS velocities fall in the range of 30–40 mm/yr near Taitung. Additionally, we find GPS velocities increase from north (~40 mm/yr) to south (~55 mm/yr) in the area affected by the Jiashian earthquake. The moving directions of GPS velocities in southwestern Taiwan are very different from the trend of plate convergence of 306° (Seno et al., 1993; Yu et al., 1997). This implies that part of the oblique motion is transferred into this region which is also justified by a large amount of strike-slip faulting as shown in Fig. 1C. We estimate the dilatation rate and principal strain-rate axes using the approach proposed by Hsu et al. (2009). The maximum rates of extension and contraction are 0.9 and −1.5 μstrain/yr, respectively (Fig. 1B). The directions of extension and contraction axes fall in the ranges of 60°–90° and 110°–140°, respectively.

On the other hand, we investigate seismicity and focal mechanism determining by first-motion polarities of P waves from Wu et al. (2010) in this area (Fig. 1C and D). The earthquakes with $M_L>2$ between 1991 and 2007 mainly occurred within a depth range of 0–20 km. A seismic gap exists near the hypocentral region of the Jiashian earthquake (Figs. 1C and 2). The focal mechanisms at depths less than 20 km indicate that the seismic deformation is mostly taken up by strike-slip and thrust faulting on the west and normal faulting on the east (Fig. 1C), consistent with strain rates derived from GPS data (Fig. 1B). We also find many earthquakes with similar focal mechanisms as the Jiashian mainshock before the mainshock (Fig. 1C). To compare with directions of strain-rate axes, we use earthquake focal mechanisms to compute the azimuth of maximum horizontal compressive stress axis (Lund and Townend, 2007). The average trend of the maximum horizontal compressive stress axes (S_H) vary from 130° to 110° and 80° from east to west (Fig. 1D). A counter-clockwise rotation of (S_H) is generally consistent with the surface GPS velocity field (Fig. 1A).

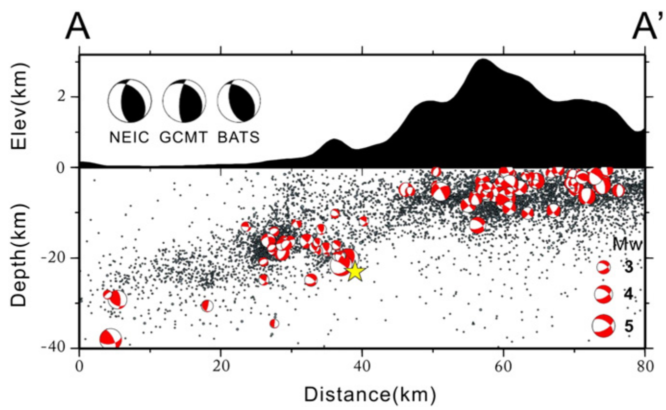

Fig. 2. A NE–SW transect of seismicity with focal depth less than 40 km between 1991 and 2007. The width of the profile is 50 km and the location is shown in Fig. 1C. The yellow star denotes the hypocenter of the Jiashian earthquake. The mainshock focal mechanism from NEIC, GCMT, and BATS are shown on top left of the figure.

3. Modeling of Coseismic Slip Distribution

3.1. GPS Data Collection and Processing

The Jiashian earthquake occurred within a pre-existing GPS network in Taiwan. The Institute of Earth Sciences, Academia Sinica (IESAS) started the construction of island-wide GPS network since 1989 (Yu et al., 1997). After the occurrence of the 1999 Chi-Chi earthquake, a dense continuous GPS (CGPS) array of more than 350 sites were installed by different institutions (Yu et al., 2003). About 108 CGPS stations locate within a radial distance of about 80 km from the epicenter of the Jiashian earthquake (Fig. 3). Most CGPS stations have recorded data for more than 5 yr before the Jiashian earthquake. The GPS data is processed using Bernese 4.2 software (Hugentobler et al., 2001) with a fiducial free approach. The daily solutions are combined into a free network solution. Precise ephemerides provided by the International GNSS Services (IGS) are employed and fixed in the post-processing. Residual tropospheric zenith delays are estimated simultaneously with the station coordinates by least-squares adjustments. The Paisha, Penghu continuous GPS station (S01R), situated on the Chinese continental margin, is chosen to define the minimum constrained conditions to its value in the International Terrestrial Reference Frame 2000 (ITRF00). The coseismic displacements were estimated from the difference between averages of 4-day GPS site positions before and after the mainshock (Table 1).

Measurements of coseismic displacements from Taiwan Continuous GPS Array indicate horizontal displacements of 5–27 mm in the NW–SW directions to the west of the epicenter; while horizontal movements to the east of the epicenter are absent (Fig. 3A). The GPS vertical displacements show an uplift motion of about 5–25 mm near the epicenter, in contrast to a small movement of about 5–10 mm observed in the far field GPS sites (Fig. 3B).

3.2. Method

The fault ruptured during the Jiashian earthquake does not extend to the surface. We approximate the fault geometry using the mainshock focal mechanisms (Fig. 2) from the Broadband Array in Taiwan for Seismology (BATS), the Global Centroid Moment Tensor (GCMT), the US Geological Survey National Earthquake Information Center (NEIC), and the first-motion polarities of P waves (Fig. 1C, Huang et al., in press). The modeled fault has a dimension of 50 km in length and

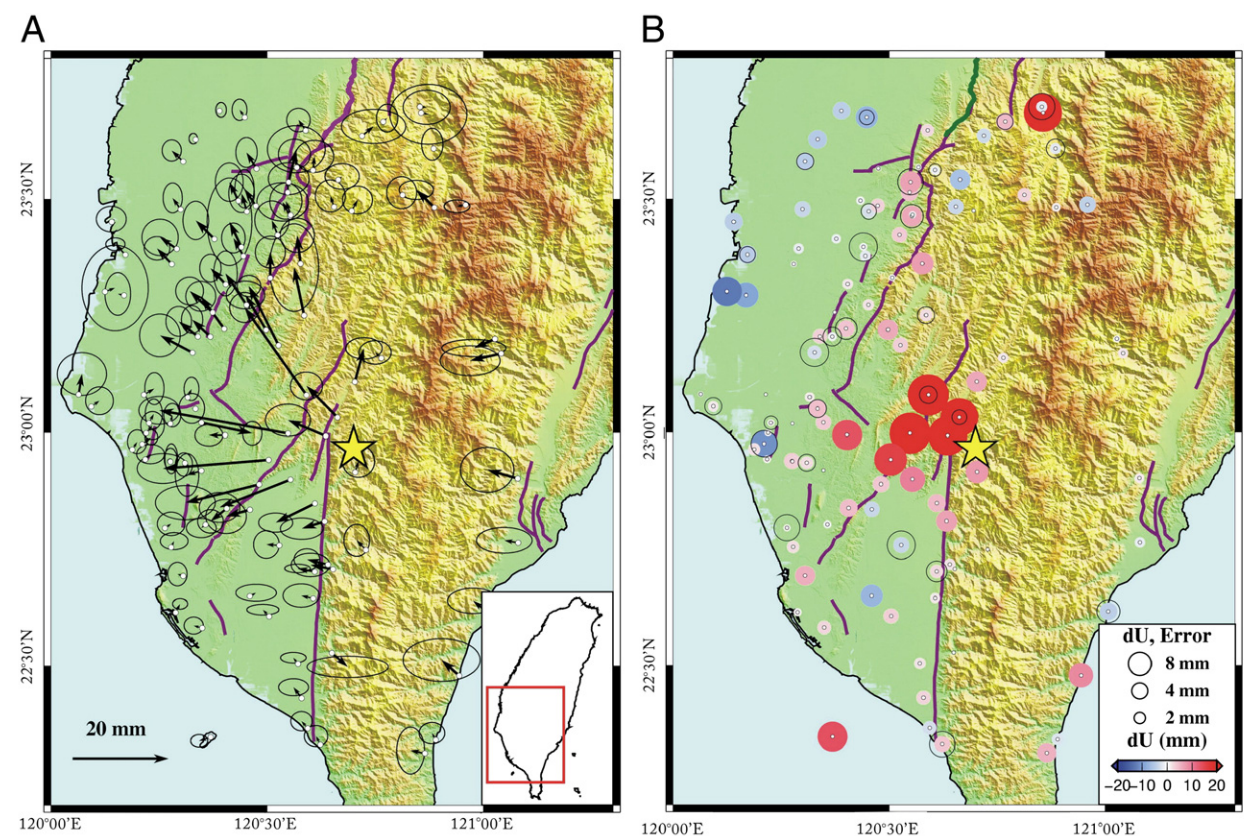

Fig. 3. Coseismic displacements of the 2010 Jiashian earthquake. (A) GPS horizontal displacements are shown in black vectors with 95% confidence ellipses. Major active faults are indicated as solid purple lines. The yellow star shows the main shock epicenter. (B) Vertical displacements are shown by circles with uplift and subsidence indicated by red and blue colors, respectively. The black circle indicates one standard deviation.

Table 1
Coseismic displacements of the Jiashian earthquake.

Site	Longitude (°)	Latitude (°)	D_E (mm)	D_N (mm)	D_U (mm)
8118	120.5530	23.4630	−1.6 ± 3.6	3.0 ± 2.7	6.4 ± 8.0
AKND	120.3573	22.8033	−0.9 ± 2.1	−0.7 ± 1.4	−0.9 ± 3.4
ALIS	120.8133	23.5082	−0.2 ± 2.1	0.5 ± 2.3	2.9 ± 3.6
BANP	120.3054	22.6931	−1.2 ± 1.4	0.4 ± 1.7	5.9 ± 5.2
BDES	120.1719	23.3806	−2.1 ± 1.4	2.2 ± 0.9	−4.9 ± 3.8
BKBL	120.0634	23.0814	0.7 ± 3.5	4.3 ± 3.0	−0.4 ± 10.0
C002	120.5772	23.3617	−0.7 ± 2.4	5.9 ± 2.4	7.2 ± 3.4
CHIA	120.4332	23.4960	−1.9 ± 2.0	3.9 ± 2.7	−1.1 ± 5.4
CHKU	120.0928	23.0558	1.7 ± 2.0	1.2 ± 2.0	1.6 ± 4.4
CHYI	120.1402	23.4508	−0.1 ± 2.1	0.6 ± 1.8	−4.8 ± 5.2
CHYN	120.2908	23.3933	−3.5 ± 2.6	2.4 ± 2.6	−1.6 ± 6.0
CISH	120.4812	22.8896	−15.4 ± 4.2	−3.8 ± 2.4	4.0 ± 7.2
CK01	120.2105	22.9759	1.9 ± 0.9	1.4 ± 1.1	−10.9 ± 10.2
CKSV	120.2200	22.9989	1.3 ± 1.7	1.6 ± 2.0	0.8 ± 5.0
CLON	120.5796	22.4301	−1.7 ± 2.1	2.3 ± 1.2	2.9 ± 9.4
CTOU	120.2778	22.7547	0.6 ± 2.0	1.3 ± 1.2	2.3 ± 6.6
CWEN	120.4528	23.4730	−1.1 ± 1.8	3.8 ± 2.7	−2.7 ± 3.6
DAJN	120.8650	22.3113	−3.0 ± 2.0	0.6 ± 3.3	5.6 ± 13.6
DASI	120.9444	22.4784	−3.7 ± 5.4	3.3 ± 3.0	8.9 ± 11.4
DAWU	120.8900	22.3406	−0.8 ± 1.8	1.4 ± 1.5	−2.2 ± 9.8
DNAN	120.4480	23.6738	−1.1 ± 1.1	1.6 ± 1.5	−7.6 ± 3.4
DONA	120.7035	22.9156	0.7 ± 2.3	2.3 ± 2.3	7.7 ± 4.2
FALI	120.5936	22.3653	−1.3 ± 1.5	1.5 ± 1.4	−2.8 ± 7.4
FKDO	120.8563	23.6836	1.5 ± 5.4	−0.3 ± 4.2	21.8 ± 21.8
GAIS	120.5906	23.0803	−12.9 ± 2.1	18.3 ± 2.1	25.1 ± 4.6
GS05	120.5684	23.5671	−0.5 ± 2.3	2.8 ± 2.1	−0.6 ± 4.4
GS06	120.5542	23.4656	−1.0 ± 2.3	2.9 ± 2.6	0.8 ± 5.8
GS07	120.6548	23.4829	−0.8 ± 2.1	2.3 ± 2.3	−3.6 ± 7.0
GS17	120.6058	23.5612	0.3 ± 2.7	2.9 ± 2.3	−1.4 ± 2.4
GS18	120.4738	23.4850	−2.4 ± 1.4	3.6 ± 2.7	3.1 ± 4.2
GS28	120.2144	23.0810	2.2 ± 1.4	1.3 ± 2.3	0.0 ± 2.2
GS29	120.3158	23.0751	0.8 ± 1.1	1.8 ± 1.7	1.3 ± 3.0
GS30	120.2263	23.0205	1.0 ± 1.2	1.9 ± 2.1	0.7 ± 2.8
GS31	120.2758	23.0189	0.4 ± 1.2	1.8 ± 1.7	−0.3 ± 2.6
GS33	120.1878	22.9644	1.0 ± 1.4	1.6 ± 1.7	2.2 ± 3.8
GS34	120.2751	22.9392	0.1 ± 0.9	0.5 ± 1.5	3.9 ± 4.8
GS35	120.3094	22.9355	−0.2 ± 1.2	−0.3 ± 1.7	2.4 ± 4.4
GS41	120.4449	23.3776	−2.1 ± 1.7	3.8 ± 2.1	−1.8 ± 5.0
GS42	120.4520	23.2732	−4.4 ± 1.7	6.6 ± 3.2	2.0 ± 8.2
GS43	120.3736	23.2572	−4.8 ± 2.0	4.5 ± 2.0	−0.3 ± 7.4
GS44	120.4004	23.2222	−4.9 ± 2.1	6.8 ± 2.1	4.2 ± 7.0
GS45	120.7282	22.7491	−1.9 ± 1.8	2.0 ± 2.3	−0.1 ± 12.8
GS46	120.6495	22.5275	3.3 ± 5.7	−2.9 ± 1.5	−0.1 ± 16.8
GS51	120.5481	22.9985	−26.9 ± 2.9	4.8 ± 2.0	25.1 ± 4.2
GS52	120.6628	23.0323	−6.5 ± 2.3	6.6 ± 2.0	21.2 ± 3.2
GS53	120.4064	22.8382	−3.4 ± 1.8	−2.7 ± 1.7	4.8 ± 5.4
GS54	120.4602	22.8354	−5.0 ± 2.9	−1.4 ± 2.4	−3.6 ± 7.8
GS55	120.6103	22.8489	−8.2 ± 2.4	−4.0 ± 1.4	5.0 ± 5.8
GS56	120.6098	22.7021	−3.6 ± 1.8	0.7 ± 0.6	2.7 ± 6.6
GUKN	120.5888	23.6459	−1.5 ± 1.7	2.2 ± 1.7	2.5 ± 5.0
ICHU	120.2793	23.3607	−3.1 ± 1.8	3.3 ± 1.7	−0.5 ± 5.0
JHCI	120.5474	23.5137	0.2 ± 2.9	2.9 ± 2.3	4.6 ± 4.6
JLUT	120.6228	22.3300	−0.9 ± 1.7	1.8 ± 1.5	4.0 ± 10.0
JONP	120.5240	23.4230	−1.2 ± 2.4	3.1 ± 2.7	3.6 ± 4.0
KASH	120.2883	22.6145	0.9 ± 1.1	1.8 ± 0.8	1.0 ± 4.6
KASU	120.6330	22.8102	−4.8 ± 3.0	−1.5 ± 1.5	6.8 ± 12.2
KAWN	120.3270	23.1712	−6.8 ± 2.9	3.6 ± 3.0	−2.8 ± 12.0
KTES	120.3343	23.6266	−0.5 ± 0.6	0.2 ± 0.8	−5.1 ± 6.0
KULN	120.5070	23.3310	0.0 ± 2.1	5.4 ± 2.3	−0.7 ± 6.8
LGUE	120.6354	22.9929	−7.9 ± 3.2	3.3 ± 2.3	22.9 ± 10.6
LIKN	120.5279	22.7586	−2.7 ± 1.8	0.2 ± 2.0	−3.8 ± 12.2
LIUC	120.3691	22.3467	−2.4 ± 1.2	−0.8 ± 0.9	13.9 ± 8.8
LNCH	120.4026	22.9946	−3.4 ± 2.0	0.0 ± 1.5	13.6 ± 3.8
MAJA	120.6521	22.7076	−4.7 ± 2.7	0.9 ± 1.7	0.1 ± 8.8
MITO	120.2632	22.7959	1.3 ± 2.0	0.9 ± 1.7	0.7 ± 10.4
MLON	120.5538	22.9000	−14.8 ± 2.9	−5.8 ± 2.1	9.7 ± 5.2
MOTN	121.0269	23.2005	−4.4 ± 4.5	−1.9 ± 1.2	−0.7 ± 10.8
NCKU	120.2758	22.9385	0.2 ± 0.9	0.6 ± 2.1	3.3 ± 6.4
NJES	120.4403	23.3970	−2.5 ± 3.2	5.3 ± 6.2	−0.9 ± 12.2
NJOU	120.5714	22.5039	−1.0 ± 1.8	1.3 ± 0.8	1.9 ± 6.6
PAOL	120.7029	23.1086	1.9 ± 2.6	7.0 ± 1.5	6.4 ± 7.6
PEIM	120.1686	23.2938	−1.3 ± 1.8	0.3 ± 3.0	−9.3 ± 3.0
PKGM	120.3055	23.5799	−2.4 ± 1.4	2.3 ± 1.5	−4.8 ± 4.2
PTUN	120.4597	22.6499	1.3 ± 2.9	0.7 ± 1.2	−7.5 ± 8.0
S011	120.3394	23.2054	−4.0 ± 1.8	3.2 ± 2.1	3.3 ± 7.0
S103	120.4752	23.5644	−2.1 ± 1.5	3.4 ± 2.1	0.4 ± 3.8
S106	120.3341	23.0508	−0.8 ± 1.8	0.1 ± 2.1	4.6 ± 4.8
S169	120.5033	22.9423	−22.1 ± 3.6	−1.8 ± 2.1	15.7 ± 5.0
S23R	120.6062	22.6450	−2.5 ± 2.6	0.6 ± 1.7	1.6 ± 5.0
SAND	120.6406	22.7173	−4.4 ± 1.8	1.1 ± 1.5	2.0 ± 14.6
SANL	120.7686	23.6645	0.8 ± 1.5	0.8 ± 2.0	5.0 ± 3.8
SCES	120.1247	23.3014	2.1 ± 4.7	0.8 ± 6.0	−12.9 ± 7.0
SGAN	120.3497	22.5813	−1.8 ± 1.4	0.5 ± 1.2	2.8 ± 6.0
SHWA	120.3478	23.0214	10.6 ± 1.4	−2.2 ± 1.7	3.7 ± 3.8
SINY	120.8532	23.6965	1.4 ± 3.3	−0.1 ± 2.4	−1.8 ± 10.2
SSUN	120.3778	23.4142	−3.9 ± 1.8	3.9 ± 2.7	−1.3 ± 5.0
SUAN	120.2999	23.4776	−1.7 ± 1.4	2.4 ± 2.1	−3.8 ± 4.0
T110	121.0799	22.9025	−6.4 ± 3.8	1.8 ± 3.2	1.5 ± 10.6
TAPU	120.5854	23.2508	−2.1 ± 3.5	10.0 ± 6.2	2.3 ± 4.2
TATA	120.8870	23.4814	−3.8 ± 2.4	3.7 ± 1.4	1.2 ± 8.4
TAYN	120.7642	23.1593	−1.3 ± 2.3	1.2 ± 1.7	1.6 ± 7.6
TKJS	120.3898	23.6880	0.3 ± 0.8	0.2 ± 1.1	−4.6 ± 2.6
TMAM	121.0075	22.6161	−2.8 ± 3.6	2.3 ± 1.8	−4.5 ± 8.0
TSLN	120.7194	23.6343	2.4 ± 4.5	2.0 ± 2.4	−3.3 ± 6.8
TTUN	121.0807	22.7646	−2.9 ± 3.9	0.5 ± 1.8	−1.6 ± 13.0
TUNS	120.4040	23.3172	−3.2 ± 1.5	3.4 ± 2.0	1.6 ± 6.8
W021	120.5495	23.5357	1.6 ± 4.1	6.9 ± 3.3	6.8 ± 10.0
W029	120.6643	23.5408	0.8 ± 2.4	0.7 ± 1.8	−6.1 ± 2.4
W030	120.6955	23.4741	1.2 ± 2.1	2.3 ± 2.0	−0.3 ± 3.6
WANC	120.5263	23.1868	−6.2 ± 1.7	12.4 ± 1.5	3.5 ± 5.4
WANS	120.8852	23.6075	−0.3 ± 1.5	0.9 ± 2.3	−1.9 ± 5.2
WDAN	120.5043	22.6061	−1.3 ± 2.3	1.4 ± 0.8	3.4 ± 9.6
WHES	120.3477	22.9192	−3.0 ± 1.7	−0.9 ± 3.0	−0.1 ± 12.8
WULU	121.0415	23.1693	−6.5 ± 4.2	−1.5 ± 2.1	1.7 ± 7.2
WUST	120.3682	23.2052	−3.8 ± 1.5	3.6 ± 2.0	−1.2 ± 5.2
YUSN	120.9591	23.4873	−1.8 ± 1.8	−0.3 ± 0.9	−4.3 ± 7.2
ZEND	120.2176	22.9433	1.1 ± 2.0	1.1 ± 1.4	0.9 ± 6.0
ZWEN	120.4973	23.2197	−4.3 ± 2.7	7.3 ± 2.0	6.2 ± 4.0

D_E, D_N, and D_U are east, north, and vertical components, respectively, of the coseismic displacement with one standard deviation.

62 km in width. The fault dips 40° to 70° and extends from the surface to 40 km at depth. To allow for spatial heterogeneous fault slip, we divide the modeled fault into 64 patches. In addition, we constrain slip directions to be left-lateral and up-dip, to be consistent with the moving directions of surface GPS coseismic displacements. A weighted least-square inversion algorithm is employed to solve for coseismic slip distribution by minimizing the following functional:

$$\boldsymbol{F}(s, \beta, \boldsymbol{m}) = \| \textstyle\sum^{-1/2} (\boldsymbol{G}(\boldsymbol{m})\boldsymbol{s} - \boldsymbol{d}) \|^2 + \beta^{-2} \| \nabla^2 \boldsymbol{s} \|^2, \quad (1)$$

where $\sum^{-1/2}$ is the inverse square root of the data covariance matrix; $\boldsymbol{G(m)}$ are Green's functions in an elastic half-space (Okada, 1985), which depend on the fault parameters $\boldsymbol{m}$; $\boldsymbol{s}$ is slip; $\boldsymbol{d}$ is the observed displacements and ∇^2 is the finite difference approximation of the Laplacian smoothing operator (Harris and Segall, 1987). The parameter of β serves as the weighting of the model roughness versus data misfit. This parameter is obtained by cross-validation (Matthews and Segall, 1993). We estimate the reduced chi-square (χ_r^2) to evaluate the goodness of the fit. A good fit is achieved with the value of χ_r^2 is about 1, meaning that the fault model fits data within uncertainties.

The causative fault of the Jiashian earthquake is ambiguous because no surface rupture was observed associated with the mainshock. We invert for coseismic slip using both nodal planes of mainshock (Figs. 1C and 2). Both models are capable of providing a satisfactory fit to GPS measurements. However, we find the NW–SE trending segment with fault dip to NE gives a smaller value of χ_r^2 (1.3) compared to the value of 1.5 using the NE–SW trending fault. Furthermore, the aftershocks projected to surface show a N300° alignment (Huang et al., in press), suggesting that a NW–SE trending fault plane is more likely to be the rupture plane during the Jiashian earthquake. We then use a grid search to find the optimal fault parameters and slip distributions. We vary fault strike from 290° to 330° and fault dip from 30° to 70° according to various focal mechanisms (Figs. 1C and 2) and the aftershock distribution. The modeling results are discussed in the next section.

3.3. Coseismic Slip Model

Our preferred fault model exhibits 0.05–0.1 m of reverse slip and ~0.04 m of left-lateral slip on a N324°-trending fault with dip of 40° to NE (Fig. 4). This fault geometry is consistent with focal mechanisms with fault strike of 310°–320° and fault dip of 40°–70° announced by Global CMT, NEIC, and BATS (Fig. 2). If we invert for coseismic slip distribution using the fault geometries from focal mechanisms instead of performing a gird search, the magnitudes of slip components and the patterns of slip distributions are not much different from the grid search result. The differences in magnitudes of strike-slip and dip-slip components are less than 15%. Our model predictions generally fit the surface GPS displacements with average residuals of 2.2, 1.2, and 3.2 mm in the east, north, and vertical components, respectively (Fig. 5). The value of χ_r^2 is 1.3 in our optimal model, implying that the model fits the data within uncertainties. However, some CGPS sites close to the rupture area show large residuals which may be related to the postseismic deformation or the limitation of using a simple elastic dislocation model. The highest slip of 0.12 m occurs to the west of the epicenter at a depth range of 15–20 km (Figs. 4 and 5) wherein the seismicity is absent before the mainshock (Fig. 5B). Given the rigidity modulus of 60 GPa, the geodetic moment is 4.95×10^{18} N-m, equivalent to a M_w 6.4 earthquake, consistent with seismic moments estimated from Global CMT, NEIC, BATS and that from seismic waveform inversion (Lee et al., in press). Additionally, the slip distribution inferred from GPS displacements is in good agreement with that in the seismic inversion (Lee et al., in press).

4. Discussion

4.1. Comparison of Orientations between Strain and Stress Axes

In our optimal model, the azimuth of slip vectors is in the range of 245°–270°, corresponding to the surface deformation pattern in Fig. 1A. Using earthquake focal mechanisms before the mainshock, we also compute the azimuth of maximum horizontal compressive axis (S_H) which represents the principal direction of horizontal maximum compressive stress (Fig. 1D). The azimuth of S_H falls in the range of 240°–290° (or 60°–110°), consistent with the trends of fault slip vectors. Although the fault structures and related activities have not been discovered before the Jiashian earthquake, the occurrence of this type of event is consistent with the regional stress field. We have found some events with the similar focal mechanism as the Jiashian mainshock in the past two decades (Fig. 1C).

4.2. Seismicity Before and After the Mainshock

Most earthquakes prior to the Jiashian mainshock occurred in the area surrounding the coseismic rupture zone (Fig. 5B). The Jiashian earthquake may be triggered by the high stress concentration in the vicinity. Previous study used the pattern informatics method (Rundle et al., 2000) computing the seismicity rate changes relative to the background seismicity and find anomalous activity near the rupture area before the Jiashian earthquake (Wu et al., 2008). However, the GPS velocity field does not show any abnormal signals before the mainshock (Fig. 1A). Due to the fluctuations of interseismic velocities within a seismic cycle, the velocity before the next large earthquake tends to be smaller than the average (Segall, 2002). It is difficult to evaluate the seismic hazard of the area without knowing the time elapsed since the last rupture.

On the other hand, the majority of aftershocks occurs within a depth range of 15–25 km and mainly occurred to the west of the hypocenter (Huang et al., in press). The N300° alignment of aftershocks in map view seems to be uncorrelated with our preferred coseismic slip model and the strike of any existing fault structure in the area. A detailed study of seismicity, earthquake focal mechanisms, and surface geology is required to explore the activities of these blind faults.

4.3. Coulomb Stress Change on Nearby Fault System

To investigate the influence of the Jiashian earthquake on nearby fault systems, we compute the Coulomb stress change on the faults in southwestern Taiwan. The Coulomb stress change is defined as, $\Delta CFS = \Delta\tau - \mu' \Delta\sigma_n$, where $\Delta\tau$ is the shear stress change on the failure

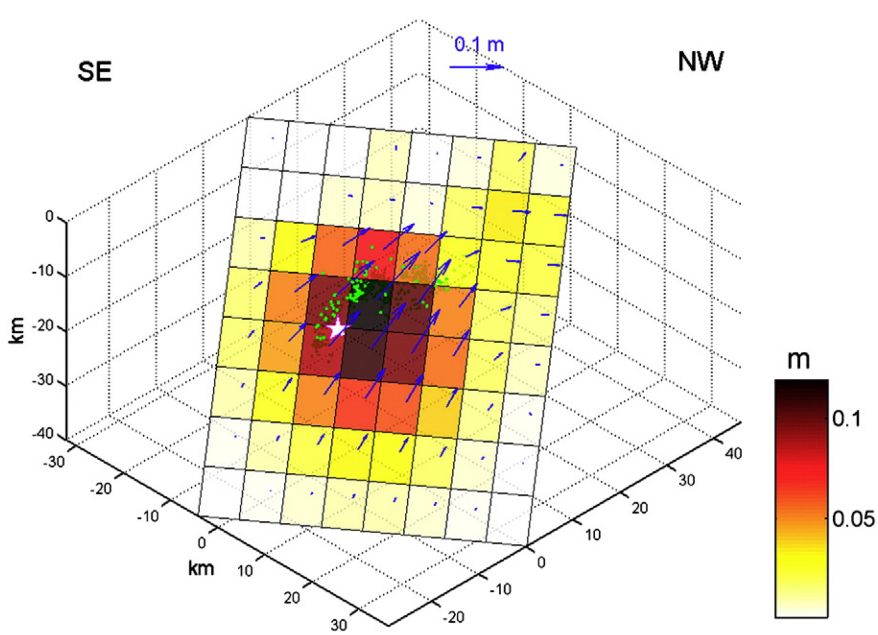

Fig. 4. Coseismic slip and fault geometry of the Jiashian earthquake. Blue vectors indicate slip rake. The amplitude of slip is shown in color. The white star and green dots denote the hypocenter and aftershocks, respectively (Huang et al., in press). The optimal fault model exhibits reverse and a small amount of left-lateral slip on a 50 km long N324°-trending segment with dip of 40° to NE.

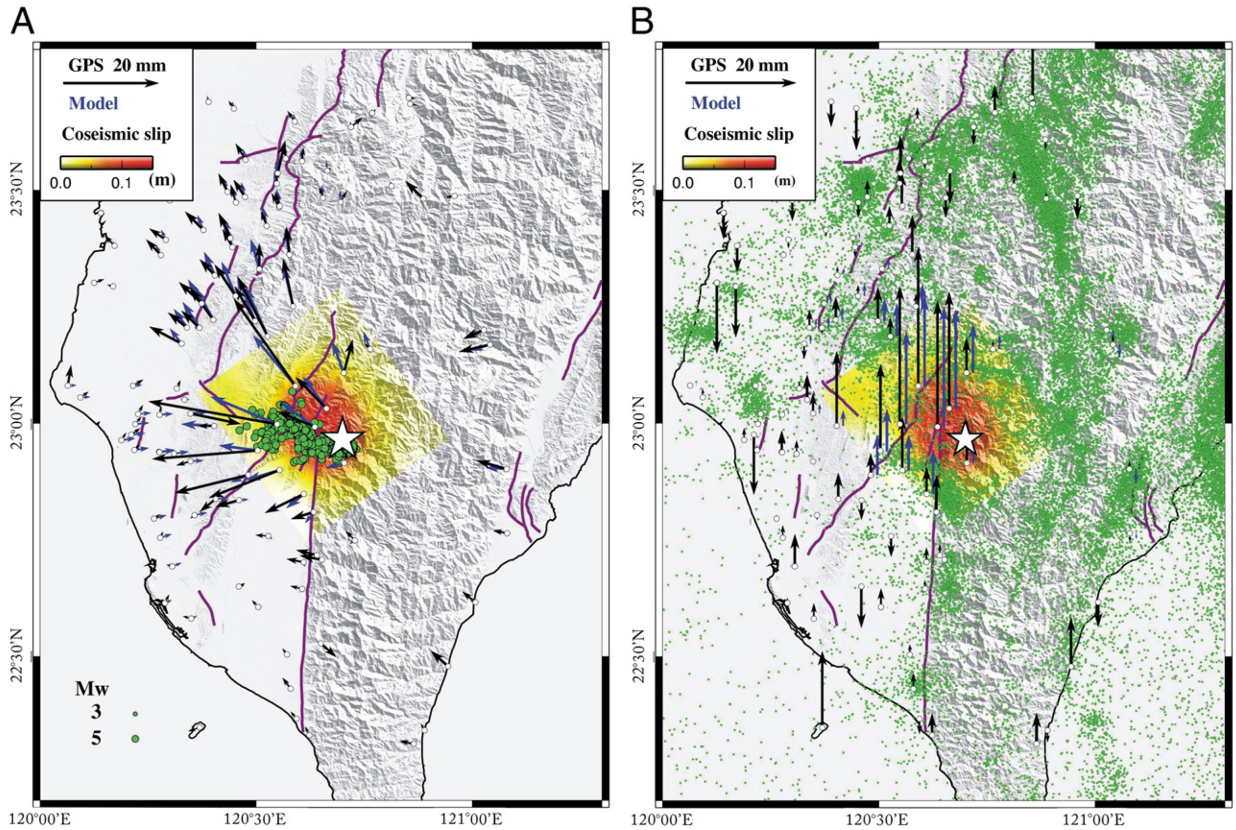

Fig. 5. The coseismic model of the Jiashian earthquake (A) Coseismic slip distribution projected on the surface is shown in color. Black and blue vectors indicate observed and model predicted GPS horizontal displacements, respectively. Major faults are indicated as solid purple lines. The white star is the main shock epicenter. Green dots denote relocated aftershocks from Huang et al. (in press). (B) Vertical displacements (black) and model predictions (blue). Green dots indicate seismicity within a depth range less than 40 km between 1991 and 2007 (Wu et al., 2010).

plane, μ' is the apparent coefficient of friction including the effect of pore-fluid change, and $\Delta\sigma_n$ is the normal stress change (clamping is positive). The fault failures are encouraged if $\Delta CFS>0$; while they are prohibited for $\Delta CFS<0$ (King et al., 1994). We estimate the stress tensor at arbitrary location using Okada's (1992) method with a Poisson ratio of 0.25 and rigidity of 60 GPa. Then we compute the shear stress and normal stress on the specified fault plane and slip direction.

The potential earthquake rupture sources near the epicenter of Jiashian earthquake include the Chaochou fault, the Chishan fault, the Hsinhua fault, and the Chukou fault (Fig. 6). The Chaochou fault separates the thick Quaternary strata in the Pingtung Plain from the Miocene-age rocks in the Central Range. The dramatic contrast of strata and the linearity of this fault in topographic map suggest that it has both vertical and strike-slip motion (Ho, 1988; Shyu et al., 2005). The NE–SW trending Chishan fault is a reverse fault with dextral motion (Lacombe et al., 2001). A significant right-lateral component of 24–30 mm/yr across the fault was inferred from the interseismic GPS velocity (Hu et al., 2007). The Hsinhua fault is a right-lateral, north-dipping fault which caused the M_w 6.3, 1946 Hsinhua earthquake in Tainan (Hsu, 1971). The fault dip varies from about 70° near the surface to 17° at great depth (Lee et al., 2000). The Chukou fault is a 30°–40° east dipping reverse fault and is also the boundary between the fold and thrust belts and the coastal plain in the Chiayi–Tainan area (Ho, 1986). The fault parameters used in the ΔCFS calculation are summarized in Table 2.

We divide these faults into small patches and calculate the Coulomb stress change on fault patches using the coseismic slip distribution of the Jiashian earthquake. The values of μ' between 0 and 0.75 are plausible (King et al., 1994). We consider a wide range of μ' from 0–0.7 and find ΔCFS does not change significantly. In addition, studies of earthquake focal mechanisms in Taiwan suggest that the friction coefficient is mostly in a range of 0.2–0.5 (Hsu et al., 2010). We decide to use the value of μ' as 0.4 for the ΔCFS computation. The results indicate that the ΔCFS are increased at the deep portion of the Chaochou fault (Fig. 6A), on most areas of the Chishan fault (Fig. 6C) and the Chukou fault (Fig. 6F). On the other hand, the ΔCFS are decreased at shallow depths of the Chaochou fault (Fig. 6A) and on the Hsinhua Fault (Fig. 6E). Most aftershocks are distributed in a small area to the west of the hypocenter at a depth range of 15–20 km (Fig. 6E). The NWW–SEE trending aftershock alignment seems to be irrelevant to the existing fault structures in the area. We decide to only plot aftershocks in Fig. 6E since only few aftershocks locate within a depth range of ±5 km of fault models listed in Table 2.

To explore the impact of fault geometries to the ΔCFS, we use a different fault dip of 60° for the Chaochou fault (Fig. 6B) and a fault dip of 60° for the Chishan fault (Fig. 6D) to calculate ΔCFS and to compare results with our preferred models constrained by geological data (Fig. 6A and B, Table 2). We find notable changes of the ΔCFS on the deep portion of the Chaochou fault and on the northern part of the Chishan fault. We thus recommend caution as to the interpretation of Coulomb stress changes. Note that the ΔCFS is also sensitive to the slip distribution and material properties; however, these issues are beyond the scope of this paper.

5. Conclusions

The occurrence of the Jiashian earthquake draws attention to the seismic hazard induced by blind thrusts in southwestern Taiwan. The evaluation of seismic hazard depends on knowing the fault geometry as well as where an earthquake will occur. Inversions of coseismic GPS displacements using the elastic dislocation theory provide constraints

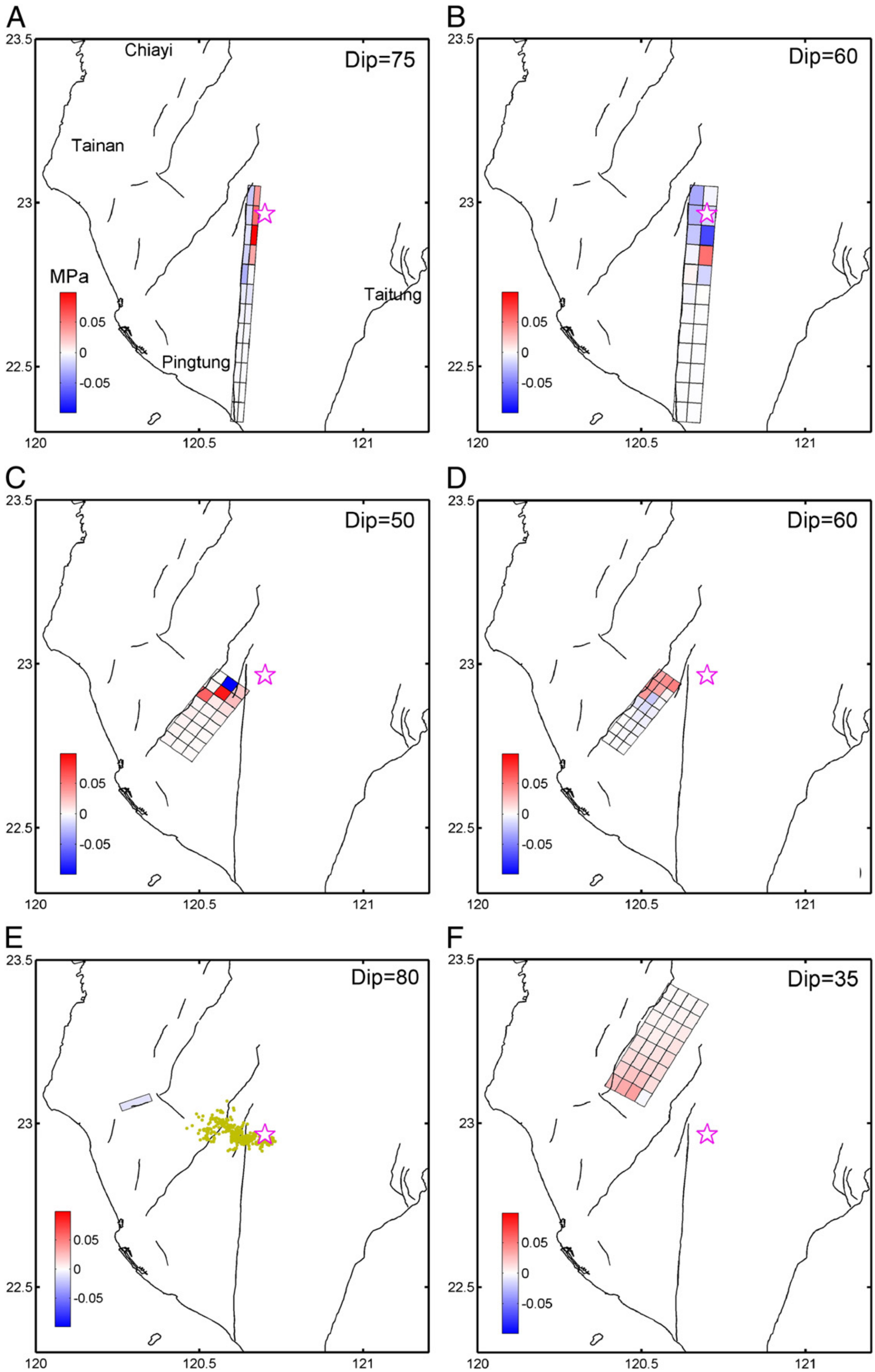

Fig. 6. Coulomb stress change (Δ*CFS*) on various fault systems. The Δ*CFS* is positive (red) if stress change promotes failures; while it is negative (blue) if stress change prohibits ruptures. (A) A 75° east-dipping Chaochou fault. (B) A 60° east-dipping Chaochou fault, (C) A 50° east-dipping Chishan fault, (D) A 60° east-dipping Chishan fault, (E) A 80° north-dipping Hsinhua Fault. Yellow dots indicate aftershocks (Huang et al., in press). (F) A 35° east-dipping Chukou fault. White star denotes the epicenter of the Jiashian earthquake.

Table 2
Fault parameters used for the Coulomb stress calculation.

Fault name	Strike (°)	Dip (°)	Rake (°)	Length (km)	Width (km)	Depth (km)
Chaochou fault	4	75	45	80	16	15
Chishan fault	37	50	120	30	20	15
Chukou fault	30	35	90	40	26	15
Hsinhua fault	250	80	180	10	15	15

on fault geometry and slip distribution. The optimal fault model exhibits a reverse slip of 0.05–0.1 m and a left-lateral slip of ~0.04 m on a N324°-trending segment with dip of 40° to NE. The highest slip of 0.12 m occurs at a depth range of 15–20 km, wherein the seismicity is absent before the mainshock. We compute the Coulomb stress changes on nearby faults to investigate the influence of stress perturbation by the mainshock. Our result suggests that the Jiashian earthquake may encourage failures on the Chukou fault and inhibit ruptures on the Hsinhua fault, whereas it shows a more complex behavior with both prompting and preventing failures on different portions of the Chaochou fault and the Chishan fault.

Acknowledgments

We thank the editor, Dr. Mian Liu, and two anonymous reviewers for their thoughtful reviews and valuable comments that helped to improve the manuscript. We are grateful to many colleagues at the Institute of Earth Sciences, Academia Sinica who have participated in collecting GPS data. The generous provision of the continuous GPS data by the Central Weather Bureau, Ministry of the Interior, Central Geological Survey, and IGS community is greatly appreciated. We thank I. G. Huang for preparing the figures in the manuscript. GMT was used to create several figures (Wessel and Smith, 1998). This is the contribution of the Institute of Earth Sciences, Academia Sinica, IESAS1539, and the National Science Council of the Republic of China grant NSC 98-2119-M-001-0330-MY3.

References

Harris, R.A., Segall, P., 1987. Detection of a locked zone at depth on the Parkfield, California, segment of the San-andreas Fault. J. Geophys. Res. 92, 7945–7962.

Ho, C.S., 1986. A synthesis of the geologic evolution of Taiwan. Tectonophysics 125, 1–16.

Ho, C.S., 1988. An Introduction to the Geology of Taiwan, Explanatory Text of the Geological Map of Taiwan, 2nd ed. Cent. Geol. Surv., Taipei, p. 192.

Hsu, M.T., 1971. Seismicity of Taiwan and some related problems. Bull. Int. Inst. Seismol. Earthquake Eng. 8, 41–60.

Hsu, Y.J., Yu, S.B., Simons, M., Kuo, L.C., Chen, H.Y., 2009. Interseismic crustal deformation in the Taiwan plate boundary zone revealed by GPS observations, seismicity, and earthquake focal mechanisms. Tectonophysics 479, 4–18.

Hsu, Y.J., Rivera, L., Wu, Y.M., Chang, C.H., Kanamori, H., 2010. Spatial heterogeneity of tectonic stress and friction in the crust: new evidence from earthquake focal mechanisms in Taiwan. Geophys. J. Int. 329–342.

Hu, J.C., Hou, C.S., Shen, L.C., Chan, Y.C., Chen, R.F., Huang, C., Rau, R.J., Chen, K.H.H., Lin, C.W., Huang, M.H., Nien, P.F., 2007. Fault activity and lateral extrusion inferred from velocity field revealed by GPS measurements in the Pingtung area of southwestern Taiwan. J. Asian Earth Sci. 31, 287–302.

Huang, H.H., Wu, Y.M., Lin, T.L., Chao, W.A., Shyu, J.B.H., Chan, C.H., Chang, C.H., in press. The preliminary study of the 4 March 2010 Mw6.3 Jiasian, Taiwan, Earthquake sequence. Terr. Atmos. Oceanic Sci. doi:10.3319/TAO.2010.12.13.01(T).

Hugentobler, U., Schaer, S., Fridez, P., 2001. Bernese GPS Software v. 4.2. Astronomical Institute, University of Berne, Switzerland. 515 pp.

King, G.C.P., Stein, R.S., Lin, J., 1994. Static stress changes and the triggering of earthquakes. Bull. Seismol. Soc. Am. 84, 935–953.

Lacombe, O., Mouthereau, F., Angelier, J., Deffontaines, B., 2001. Structural, geodetic and seismological evidence for tectonic escape in SW Taiwan. Tectonophysics 333, 323–345.

Lee, C.T., Chen, C.T., Chi, Y.M., Liao, C.W., Liao, C.F., Lin, C.C., 2000. Engineering Investigation of Hsinhua Fault, vol. 7. National Central University (in Chinese).

Lee, S.J., Liang, W.T., Mozziconacci, L. Hsu, Y.J., Lu, C.Y., Huang, W.G., Huang, B.S., in press. Source complexity of the 4 March 2010 JiaSian, Taiwan earthquake determined by joint inversion of teleseismic and near-field data. Geophys. J. Int. (revised).

Lund, B., Townend, J., 2007. Calculating horizontal stress orientations with full or partial knowledge of the tectonic stress tensor. Geophys. J. Int. 170, 1328–1335.

Matthews, M.V., Segall, P., 1993. Estimation of depth-dependent fault slip from measured surface deformation with application to the 1906 San-Francisco earthquake. J. Geophys. Res. 98, 12153–12163.

Okada, Y., 1985. Surface deformation due to shear and tensile faults in a half-space. Bull. Seismol. Soc. Am. 75, 1135–1154.

Okada, Y., 1992. Internal deformation due to shear and tensile faults in a half-space. Bull. Seismol. Soc. Am. 82, 1018–1040.

Rundle, J.B., Klein, W., Tiampo, K., Gross, S., 2000. Linear pattern dynamics in nonlinear threshold systems. Phys. Rev. E 61, 2418–2431.

Segall, P., 2002. Integrating geologic and geodetic estimates of slip rate on the San Andreas fault system. Int. Geol. Rev. 44, 62–82.

Seno, T., Stein, S., Gripp, A.E., 1993. A model for the motion of the Philippine Sea Plate consistent with Nuvel-1 and geological data. J. Geophys. Res. 98, 17941–17948.

Shyu, J.B.H., Sieh, K., Chen, Y.G., Liu, C.S., 2005. Neotectonic architecture of Taiwan and its implications for future large earthquakes. J. Geophys. Res. 110. doi:10.1029/2004JB003251.

Wessel, P., Smith, W.H.F., 1998. New, improved version of Generic Mapping Tools released. EOS Trans. AGU 79 (47), 579.

Wu, Y.H., Chen, C.C., Rundle, J.B., 2008. Precursory seismic activation of the Pingtung (Taiwan) offshore doublet earthquakes on 26 December 2006: a pattern informatics analysis. Terrestrial Atmos. Oceanic Sci. 19, 743–749.

Wu, Y.M., Hsu, Y.J., Chang, C.H., Teng, L.S., Nakamura, M., 2010. Temporal and spatial variation of stress field in Taiwan from 1991 to 2007: insights from comprehensive first motion focal mechanism catalog. Earth Planet. Sci. Lett. 298, 306–316.

Yu, S.B., Chen, H.Y., Kuo, L.C., 1997. Velocity field of GPS stations in the Taiwan area. Tectonophysics 274, 41–59.

Yu, S.B., Hsu, Y.J., Kuo, L.C., Chen, H.Y., Liu, C.C., 2003. GPS measurement of postseismic deformation following the 1999 Chi-Chi, Taiwan, earthquake. J. Geophys. Res. 108. doi:10.1029/2003JB002396.